A PRIORI TESTS OF TURBULENCE MODELS FOR COMPRESSIBLE FLOWS

A. Cannici[(1)], D. Passiatore[(2)], L. Sciacovelli[(3)] and P. Cinnella[(4)]

[(1)]Arts et Métiers, DynFluid Laboratory, 151 Boulevard de l'Hopital, 75013 Paris France, aron.cannici@onera.fr

[(2)]Politecnico di Bari, DMMM, via Re David 200, 70125 Bari Italy, donatella.passiatore@poliba.it

[(3)]Arts et Métiers, DynFluid Laboratory, 151 Boulevard de l'Hopital, 75013 Paris France, luca.sciacovelli@ensam.eu

[(4)]Sorbonne Université, Institut d'Alembert, 4 Place Jussieu, 75005 Paris France, paola.cinnella@sorbonne-universite.fr

ABSTRACT

The present work reports the results of a priori tests of Reynolds-Averaged Navier–Stokes (RANS) models based on Direct Numerical Simulations (DNS) data of zero-pressure-gradient flat-plate turbulent boundary layers. The DNS database covers a wide range of thermodynamic operating flow conditions, from supersonic ($M_\infty = 2.25$) up to the high-enthalpy hypersonic regime ($M_\infty = 12.48$). The most common RANS closures and compressibility corrections in literature are assessed against the exact terms from the DNS. Particular attention has been paid to closure models for the turbulent heat fluxes and the dilatational dissipation, as well as to the analysis of turbulence/chemistry and turbulence/vibrational relaxation interactions for the high-enthalpy simulations.

1. INTRODUCTION

The study of high-speed flows is of critical importance in the field of aeronautics and astronautics. Vehicles travelling at supersonic and hypersonic speeds, such as reentry capsules and ballistic missiles, experience extreme mechanical and thermal loads due to aerodynamic effects; fundamental understanding of the flow conditions through high-fidelity numerical simulations or experimental measurements allows for accurate prediction of those loads. As the flow transitions to turbulence, a significant increase in skin friction and wall heat fluxes occurs, making it even more crucial to accurately describe the flow behavior. Generally, numerical simulations of turbulent flows for industrial applications are mainly conducted using Reynolds-Averaged Navier–Stokes (RANS) models, most of which have been designed and calibrated for incompressible flows. When dealing with compressible configurations, the most common approach is to account for variable density and transport properties by Favre-averaging the Navier–Stokes equations. This gives rise to several unclosed terms not present in the RANS equations for incompressible, constant-property flows, which are very often neglected. While this approach provides acceptable results at low supersonic Mach numbers, it becomes unsuitable when compressibility and/or non-equilibrium effects become relevant. Attempts of developing RANS closures well-suited to the compressible regime exist in the literature, but they are derived from relatively-simple canonical configurations, such as homogeneous isotropic turbulence or mixing layers. Relevant examples in literature are the works of Sarkar *et al.* [14] and Zeman [19] which introduced the concept of dilatational dissipation for compressible turbulence and incorporated it in a closure model for mixing layers. Later on, Wilcox [17] extended this concept to flat-plate boundary layers and proposed a modification of the k-ω model for compressible flows. Catris and Aupoix [2] introduced a density scaling in the diffusion terms of turbulent transport equations to account for variable flow properties across high-speed boundary layers due to friction heating. More recently, Pecnick and Patel [12] investigated variable-property scalings for non-adiabatic turbulent channel flows, and obtained a new scaling of the diffusion terms [7] rather similar to that of [2]. An extensive assessment of turbulence models for compressible turbulent flows was conducted in the review paper of Roy [13], showing that while some of the turbulence models do provide reasonable predictions for the surface pressure, the predictions for surface heat flux are generally poor, and often in error by a factor of four or more. Overall, closure models for the compressible RANS equations

remain an open subject of research. The closure problem is even more complex for high-enthalpy regimes, where thermochemical non-equilibrium effects such as dissociation/recombination and vibrational relaxation processes may play an important role in the overall flow dynamics and have to be accounted for. The closure of the additional unclosed terms for turbulent transport of chemical species or vibrational energy introduces additional uncertainties in RANS approaches, which are not well-quantified yet, due to the lack of reference data.

Performing physical experiments in these extreme flow conditions is generally a costly or even infeasible task, whence the interest of leveraging high-fidelity approaches and specifically Direct Dumerical Simulations (DNS). DNS is computationally expensive and usually limited to simple geometries and low Reynolds numbers, and this is even more true for high-enthalpy hypersonic flows, for which additional transport equations for the chemical species in the reacting mixture and for thermal non-equilibrium must be solved alongside the standard equations for mass, momentum, and total energy. Despite these limitations, DNS represents an invaluable resource for fundamental understanding of turbulence dynamics and for the assessment of RANS models. Recently, our team has generated some of the very first DNS for high-enthalpy hypersonic flows out of chemical or thermochemical equilibrium [10, 11]. The results showed the presence of a marked interaction between turbulence and non-equilibrium conditions; specifically, vibrational relaxation and chemical dissociation processes are promoted and sustained by the onset of turbulent motions. As a consequence, the classical approach of neglecting turbulence/thermochemistry interactions underestimates the source terms for the chemical production rates and the translational-vibrational energy exchanges. Additionally, the lack of properly-designed closures for the turbulent fluxes of the species and vibrational energy equations lead us to investigate the behaviour of the simplified existing models for these configurations, motivating the present study. Precisely, the objective of this work is to quantify the deficiencies of RANS models by means of a priori tests using a database of several DNS of zero-pressure-gradient flat-plate turbulent boundary layers (TBL) spanning from supersonic to high-enthalpy hypersonic conditions [16, 10, 11].

The structure of the paper is as follows: the numerical databases are presented in section 2; section 3 presents the averaged equations and the main closure models investigated. Results are then shown in section 4 and conclusive remarks and perspectives are listed in section 5.

2. NUMERICAL DATABASES

Five different DNS databases are considered in this work, spanning a wide range of thermodynamic conditions from the supersonic ($M_\infty = 2.25$) up to the hypersonic, high-enthalpy regime ($M_\infty = 12.48$). Details about the free-stream and boundary conditions, the number of grid points and the extent of the computational domains are given in table 1. In the M2 and M6 runs, air is modeled as a single-species thermally- and calorically-perfect gas (see [15]), whereas simulations M10F, M10C and M12 make use of a thermally-perfect five-species mixture of N_2, O_2, NO, N and O. Non-catalytic wall conditions are considered for all the multi-species cases. Run M10C uses finite-rate chemistry models [16], whereas M10F is performed with a frozen-chemistry assumption (unpublished data set; a similar calculation using the same gas model and a somewhat different numerical setting can be found in [10]). Lastly, case M12 considers the contextual presence of vibrational and chemical nonequilibrium. All the test cases are spatially-evolving boundary layers initiated at a specific inlet Reynolds number; transition to turbulence is triggered by means of suction and blowing strategy. The interested reader might refer to [15, 16, 11] for details about the governing equations and the numerical schemes used in the simulations. In order to carry out comparisons, profiles were extracted at streamwise stations corresponding to well-developed turbulent flow. Due to the very different flow conditions, the friction Reynolds numbers $Re_\tau = \overline{\rho}_w u_\tau \delta_{99} / \overline{\mu}_w$ of the considered simulations do not match. Nevertheless, profiles of the turbulent statistics were found to exhibit reasonable self-similarity at the chosen stations. Some properties of the stations selected for the analysis are given in table 2.

Figure 1 displays wall-normal profiles of the turbulent Mach number $M_t = \sqrt{u_i'^2}/\overline{c}$ (u_i being the velocity fluctuations and c the speed of sound), the normalized temperature fluctuations and the density fluctuations in the top, middle and bottom panel, respectively, against the semi-locally scaled wall distance $y^\star$. In all cases, M_t is shown to peak in the buffer layer and its values get larger with the increasing free-stream Mach number. The much larger M_t registered for the M12 case is due to the presence of a significant wall cooling imposed by the isothermal wall condition, which is also responsible of the peak of temperature fluctuations in the inner region. Furthermore, the strong near-wall temperature gradient leads in turn to increased density fluctuations towards the wall. The global maximum of the thermodynamic fluctuations is achieved close to the boundary layer edge, owing to the strong intermittency caused by the alternation of turbulent bulges and laminar-like flow regions. M10F and M10C runs display larger variations with respect to M12 because of the much smaller free-stream temperature. Since chemical dissociation reactions are of endothermic nature, the mean temperature values $\overline{T}$ for M10C tend to be smaller than those for M10F, leading to higher fluctuation levels for the former.

Table 1: Parameters of the DNS considered for the tests. M_∞, T_∞ and P_∞ denote the free-stream Mach number, temperature and pressure, respectively. T_w lists the isothermal/adiabatic wall boundary condition for each case; N_x, N_y and N_z represent the number of grid points in the streamwise, wall-normal and spanwise direction; L_x, L_y and L_z are the extents of the computational domains, δ_{99} and δ^*_{in} being the thickness and the displacement thickness of the boundary layer at the inflow section, respectively.

Case	M_∞	T_∞ [K]	P_∞ [Pa]	T_w [K]	N_x	N_y	N_z	L_x	L_y	L_z
M2 [16]	2.25	65	2422	$T_w = 120.2$	8000	300	512	1600 $\delta^\star_{in}$	100 $\delta^\star_{in}$	62.83 π $\delta^\star_{in}$
M6 [15]	6	78	2421.3	$T_w = 422.5$	7700	300	400	75.2 δ_{99}	2.13 δ_{99}	2.17 δ_{99}
M10F	10	350	3596.0	Adiabatic	5520	256	240	8000 $\delta^\star_{in}$	320 $\delta^\star_{in}$	100 π $\delta^\star_{in}$
M10C [16]	10	350	3596.0	Adiabatic	5520	256	240	8000 $\delta^\star_{in}$	320 $\delta^\star_{in}$	100 π $\delta^\star_{in}$
M12 [11]	12.48	594.3	4656.0	$T_w = 1800$	9660	480	512	3000 $\delta^\star_{in}$	120 $\delta^\star_{in}$	30 π $\delta^\star_{in}$

Table 2: Data from the DNS at the streamwise stations selected for the analysis. Streamwise Reynolds number Re_x, friction Reynolds number Re_τ, momentum-thickness-based Reynolds number Re_θ, friction Mach number Ma_τ, and grid resolutions in the streamwise (Δx^+), wall-normal (Δy^+) and spanwise (Δz^+) directions, respectively.

Case	$Re_x \cdot 10^{-6}$	Re_τ	Re_θ	Ma_τ	Δx^+	Δy^+	Δz^+
M2 [16]	2.56	589.6	3531	0.075	4.4	0.59	2.7
M6 [15]	11.8	401.8	5960	0.122	3.8	0.26	2.1
M10F	48.1	213.5	10875	0.154	3.7	0.42	3.4
M10C [16]	48.1	244.1	10411	0.157	4.5	0.50	4.1
M12 [11]	15.2	984.3	5491	0.213	7.6	0.67	4.5

3. EQUATIONS AND MODELS

3.1 Favre-averaged Navier–Stokes

The basis of compressible turbulence models are the Favre-averaged (i.e., density-weighted) compressible Navier–Stokes (NS) equations:

$$\frac{\partial \overline{\rho}}{\partial t} + \frac{\partial (\overline{\rho}\widetilde{u}_i)}{\partial x_i} = 0 \tag{1}$$

$$\frac{\partial \overline{\rho}\widetilde{u}_i}{\partial t} + \frac{\partial \overline{\rho}\widetilde{u}_i\widetilde{u}_j}{\partial x_j} = -\frac{\partial \overline{p}}{\partial x_i} + \frac{\partial}{\partial x_j}\left(\overline{\tau}_{ij} - \overline{\rho u_i'' u_j''}\right) \tag{2}$$

$$\begin{aligned}
&\frac{\partial}{\partial t}\left[\overline{\rho}\widetilde{E} + \frac{\overline{\rho u_i'' u_i''}}{2}\right] + \frac{\partial}{\partial x_j}\left[\overline{\rho}\widetilde{u}_j\left(\widetilde{H} + \frac{\overline{\rho u_i'' u_i''}}{2}\right)\right] \\
&= -\frac{\partial}{\partial x_j}\left[\overline{q}_j + \overline{\rho u_j'' h''}\right] + \frac{\partial}{\partial x_j}\left[\overline{\tau_{ij} u_i''} - \overline{\rho u_j'' \frac{1}{2} u_i'' u_i''}\right] \\
&+ \frac{\partial}{\partial x_j}\left[\left(\overline{\tau}_{ij} - \overline{\rho u_i'' u_j''}\right)\widetilde{u}_j\right]
\end{aligned} \tag{3}$$

where t and x_i denotes the time and space coordinates, u_i the velocity components, p the pressure and τ_{ij} the viscous stress tensor; $E = e + \frac{1}{2}u_i u_i$ the specific total energy (e being the specific internal energy), H the total enthalpy and q_j the heat flux. In the momentum and total energy equations (2)-(3), the Favre-averaged Reynolds stress tensor $\tau^R_{ij} = \overline{\rho u_i'' u_j''}$ appears; other unclosed terms are the turbulent kinetic energy $\overline{\rho}k = \frac{1}{2}\overline{\rho u_i'' u_i''}$, the turbulent heat flux $q^{\mathrm{t}}_j = \overline{\rho u_j'' h''}$, the molecular diffusion $\overline{\tau_{ij} u_i''}$ and the turbulent transport of turbulent kinetic energy $\overline{\rho u_j'' \frac{1}{2} u_i'' u_i''}$.

When the operating conditions are such that the flow enters in a chemical non-equilibrium regime, air can no longer be considered as an homogeneous thermally and calorically-perfect gas. A mixture of five species is considered, namely, N_2, O_2, NO, N and O; the NS equations are therefore complemented with species conservation equations, here given in instantaneous form:

$$\frac{\partial \rho_n}{\partial t} + \frac{\partial (\rho_n u_j)}{\partial x_j} = -\frac{\partial \rho_n u^D_{nj}}{\partial x_j} + \dot{\omega}_n \tag{4}$$

where $\rho_n = \rho Y_n$ is the partial density of the n-th species (Y_n being mass fraction), u^D_{nj} the n-th species diffusion velocity and $\dot{\omega}_n$ the chemical production rate.
In thermal non-equilibrium conditions, vibrational relaxation processes should also be considered. Following the two-temperature (2T) model of Park [9], these processes are taken into account by adding a conservation equation for the vibrational energy e_V:

$$\begin{aligned}
\frac{\partial \rho e_V}{\partial t} + \frac{\partial \rho e_V u_j}{\partial x_j} =& \frac{\partial}{\partial x_j}\left(-q_{Vj} - \sum_{m=1}^{\mathrm{NM}} \rho_m u^D_{mj} e_{Vm}\right) \\
&+ \sum_{m=1}^{\mathrm{NM}} \left(Q_{\mathrm{TV}m} + \dot{\omega}_m e_{Vm}\right)
\end{aligned} \tag{5}$$

Here, NM is the number of molecular species (NM = 3 in the current analysis), q_{Vj} the vibrational contribution

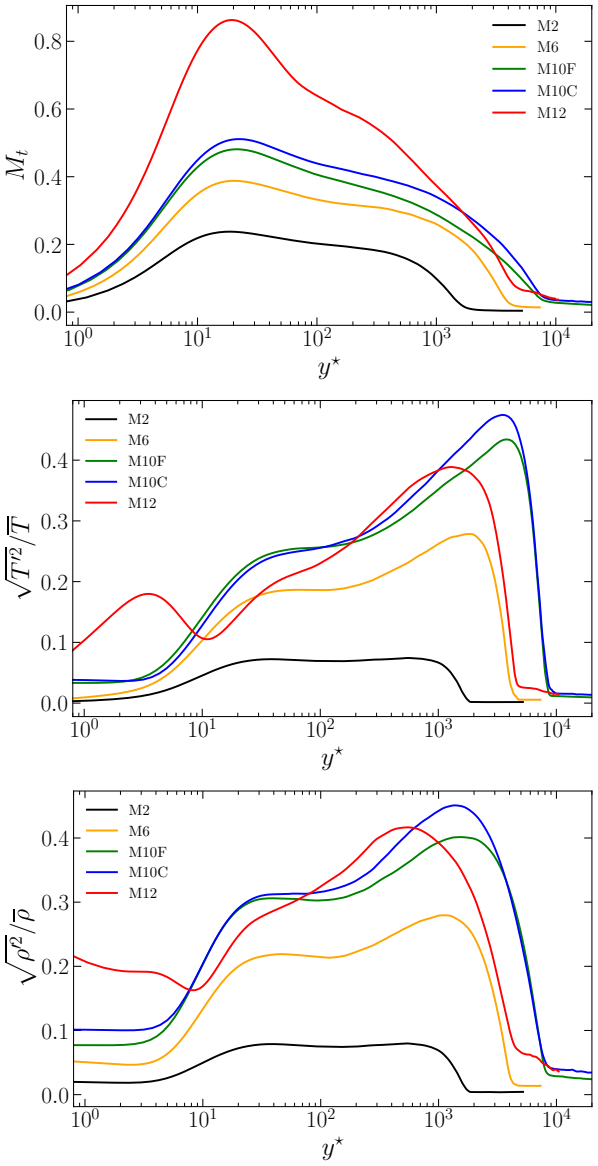

Figure 1: Wall-normal profiles of turbulent Mach number M_t, normalized temperature fluctuations $\sqrt{\overline{T'^2}}/\overline{T}$ and normalized density fluctuations $\sqrt{\overline{\rho'^2}}/\overline{\rho}$ from the DNS database at the stations listed in table 2.

of the heat flux and e_{V_m} the vibrational energy per unit of volume of the m-th species. The latter is given by

$$e_{Vm} = \frac{\theta_m R_m}{\exp(\theta_m/T_V) - 1}, \tag{6}$$

θ_m being the characteristic vibrational temperature of each molecule, R_m the gas constant and T_V the vibrational temperature. Lastly, Q_{TV} and $\dot{\omega}_m e_{Vm}$ are source terms denoting translational-vibrational energy exchanges and the vibrational energy variations due to chemical production/depletion, respectively. Additional information about the 2T model can be found in [11].

Favre-averaging of equations (4) and (5) results in additional unclosed terms, not given here for the sake of brevity. The most relevant ones, i.e. turbulent transport of species and vibrational energy and the Favre-averaged source terms, are discussed in Sections 4.4 and 4.5.

3.2 Turbulence closure models

Throughout this work we solely focus on so-called eddy-viscosity models, largely employed in engineering applications. These models rely on the so-called Boussinesq approximation to express the constitutive law for the Reynolds stresses:

$$\overline{\rho}\,\tau_{ij}^R = 2\mu_t\left(\overline{S}_{ij} - \frac{1}{3}\overline{S}_{kk}\delta_{ij}\right) - \overline{\rho}\frac{2}{3}k\delta_{ij} \tag{7}$$

where μ_t is the eddy viscosity, $\overline{S}_{ij}$ the mean strain-rate tensor and δ_{ij} the Kronecker symbol. Such an approximation reduces the modeling problem to the calculation of a single scalar, μ_t. Hereafter we consider so-called two-equation models, which express μ_t as a function of two turbulent variables allowing to determine a turbulent length and velocity scale. For each of them a transport equation is written in order to calculate the eddy viscosity. The first variable is generally the turbulent kinetic energy k, for which an exact transport equation can be derived from the momentum equation (see section 4.2).

The turbulent heat fluxes are generally modelled through a "turbulent Fourier law":

$$q_j^{\mathrm{t}} = -\frac{\mu_t c_p}{Pr_t}\frac{\partial \widetilde{T}}{\partial x_j} \tag{8}$$

where Pr_t is the turbulent Prandtl number, most often assumed to be constant equal to 0.9 for turbulent air flows. In practice, this parameter is case-dependent and varies throughout the flow. In [11], a "vibrational Fourier law" is proposed to model the corresponding term in the vibrational energy equation.

Similarly, turbulent mass fluxes arising in the Favre-averaged species transport are modelled through a turbulent Fick law by introducing again a, supposedly constant, turbulent Schmidt number Sc_t. For passive scalar transport, the turbulent Schmidt and Prandtl number coincide, so that a common approximation consists in setting $Sc_{t,n} \approx 0.9$ for all species.

4. A PRIORI TESTS

The validity of the above-mentioned assumptions, as well as supplementary assumptions used to close the turbulent kinetic energy transport equation are assessed against the exact unclosed terms extracted from the DNS statistics.

4.1 Eddy viscosity and Reynolds stresses

First, we discuss the validity of linear constitutive laws adopted for the Reynolds stresses, turbulent heat fluxes,

and mass fluxes. The constitutive relation adopted for the Reynolds stresses is a linear eddy viscosity model (LEVM), of the form $\mu_t = \rho C_\mu \ell_t v_t$, where ℓ_t and v_t are the characteristic length and velocity scales of turbulent structures, respectively, and C_μ a model constant to be defined. The eddy viscosity coefficient is computed according to the SST k-ω model [6]. The model transport equations in conservative form are

$$\frac{\partial \overline{\rho} k}{\partial t} + \frac{\partial \overline{\rho} k \widetilde{u}_j}{\partial x_j} = \tau_{ij}^R \frac{\partial \widetilde{u}_i}{\partial x_j} - \beta^* \rho \omega k + \frac{\partial}{\partial x_j}\left[(\overline{\mu} + \sigma_k \mu_t)\frac{\partial k}{\partial x_j}\right] \tag{9}$$

$$\frac{\partial \overline{\rho} \omega}{\partial t} + \frac{\partial \overline{\rho} \omega \widetilde{u}_j}{\partial x_j} = \frac{\overline{\rho}\gamma}{\mu_t}\tau_{ij}^R \frac{\partial \widetilde{u}_i}{\partial x_j} - \overline{\rho}\beta\omega^2 + \frac{\partial}{\partial x_j}\left[(\overline{\mu} + \sigma_\omega \mu_t)\frac{\partial \omega}{\partial x_j}\right] + 2(1-F_1)\frac{\overline{\rho}\sigma_{\omega 2}}{\omega}\frac{\partial k}{\partial x_j}\frac{\partial \omega}{\partial x_j} \tag{10}$$

In figure 2 we report the "exact" eddy viscosity coefficient, computed as:

$$\mu_t \approx -\overline{\rho}\widetilde{u''v''}\left(\frac{\partial \widetilde{u}}{\partial y}\right)^{-1} \tag{11}$$

and the modelled μ_t computed from the DNS data:

$$\mu_t = \frac{\overline{\rho} a_1 k}{\max(a_1\omega, SF_2)} \tag{12}$$

where we use the k and ω resulting from the DNS statistics. For the simple sheared flow at stake, the shear stress dominates the wall normal components, and the LEVM eddy viscosity (top panel) follows reasonably well the exact one for cases M2, M6 and also for the frozen-chemistry case M10F, indicating the effects of increasing friction heating are well-captured by the model overall. More significant deviations are observed for the finite-rate chemistry, adiabatic wall case M10C, for which the SST-model overpredicts the eddy viscosity significantly. For such a case, the endothermic chemical reactions drain part of the energy supplied by the mean field, leading to reduced turbulent kinetic energy compared to the corresponding frozen case [10] and altering to some extent the near-wall characteristic time scales. The largest discrepancies are obtained for the M12 case, for which thermal non-equilibrium effects combine with severe wall cooling. For this case, not only the near-wall profiles differ, but even larger deviations are observed at the boundary layer edge. In this region, turbulent velocity fluctuations vanish, but still fluctuating stress persist as an effect of the strong acoustic radiation outside the boundary layer. Note that since k and ω are directly obtained from DNS data, the above-mentioned discrepancies can be attributed to the expression used for μ_t, and specifically to the empirical function F_2. In contrast, as expected for a LEVM,

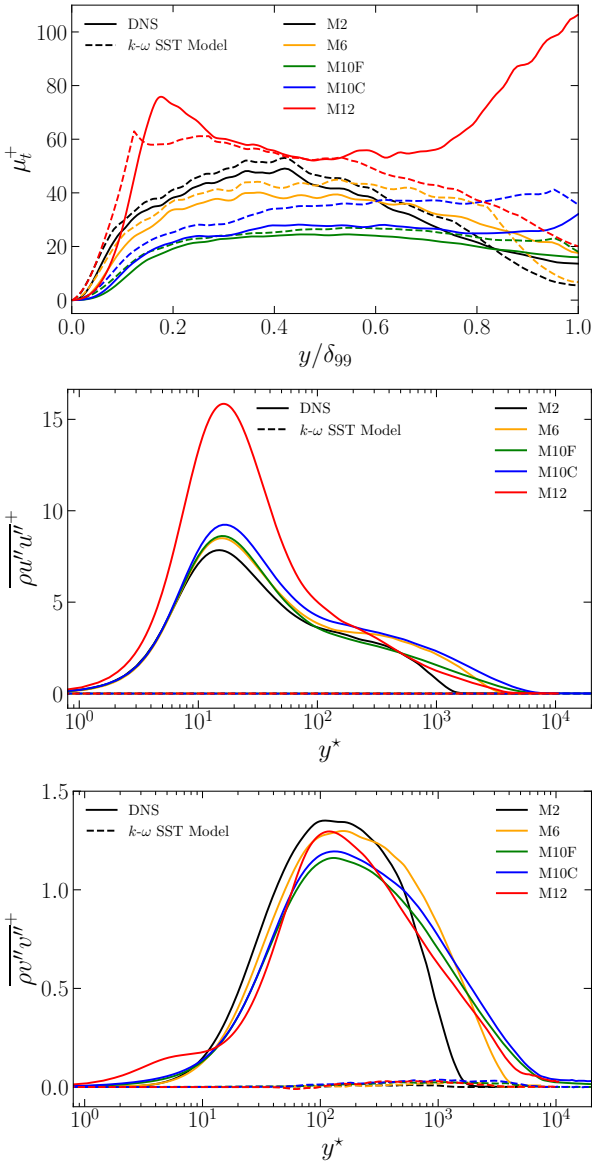

Figure 2: Exact μ_t^+ and Reynolds stresses from DNS versus their modelled counterparts.

the normal components reconstructed from the Boussinesq model are severely underestimated.

4.2 Turbulent Kinetic Energy equation

Next, we assess the validity of models used for the closure of the turbulent kinetic energy equation. In the compressible case, this takes the form:

$$\overline{\rho}\frac{\partial k}{\partial t} + \overline{\rho}\widetilde{u}_j\frac{\partial k}{\partial x_j} = \overline{\rho}\tau_{ij}^R\frac{\partial \widetilde{u}_i}{\partial x_j} - \overline{\tau_{ij}\frac{\partial u_i''}{\partial x_j}} + \frac{\partial\left[\overline{\tau_{ji}u_i''} - \overline{\frac{1}{2}\rho u_j'' u_i'' u_i''} - \overline{p' u_j''}\right]}{\partial x_j} - \overline{u_i''}\frac{\partial \overline{p}}{\partial x_i} + \overline{p'\frac{\partial u_i''}{\partial x_i}} \tag{13}$$

In the above, several unclosed terms appear, some of which are counterparts of those already present in the in-

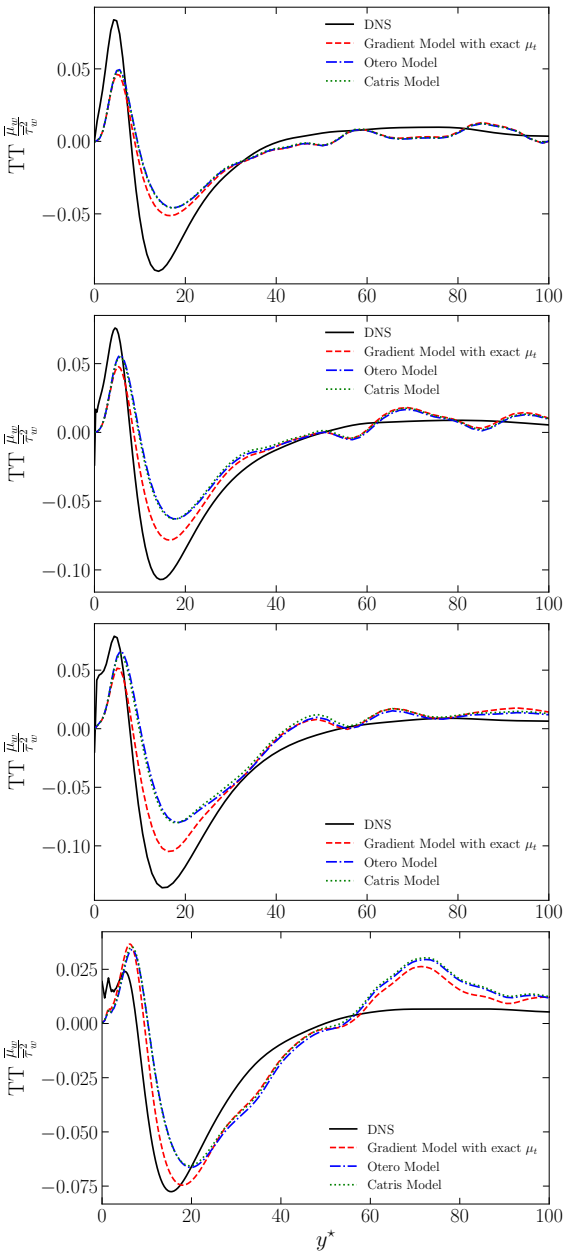

Figure 3: Turbulent transport of k, comparison of the exact term with the models. From top to bottom: M2, M6, M10C and M12.

compressible k formulation. Some other, related to compressibility effects, also need to be modelled. The term $\frac{\partial}{\partial x_j}(\overline{\frac{1}{2}\rho u_j'' u_i'' u_i''})$, referred-to as turbulent transport (TT) of k, is traditionally modeled by means of a gradient approximation:

$$\frac{\partial}{\partial x_j}\left(\overline{\frac{1}{2}\rho u_j'' u_i'' u_i''}\right) \approx \frac{\partial}{\partial x_j}\left(\frac{\mu_t}{\sigma_k}\frac{\partial k}{\partial x_j}\right) \tag{14}$$

where σ_k is a closure coefficient. For high-M flows, density gradients influence the logarithmic region of the velocity profile and must be accounted for in order to recover the correct near-wall behaviour. A compressibility correction for density variations was initially proposed by Catris & Aupoix [2]:

$$\frac{\partial}{\partial x_j}\left(\overline{\frac{1}{2}\rho u_j'' u_i'' u_i''}\right) \approx \frac{\partial}{\partial x_j}\left(\frac{1}{\overline{\rho}}\frac{\mu_\tau}{\sigma_k}\frac{\partial \overline{\rho} k}{\partial x_j}\right) \tag{15}$$

and later refined by Otero et al. [8]:

$$\frac{\partial}{\partial x_j}\left(\overline{\frac{1}{2}\rho u_j'' u_i'' u_i''}\right) \approx \frac{1}{\sqrt{\overline{\rho}}}\frac{\partial}{\partial x_j}\left(\frac{1}{\sqrt{\overline{\rho}}}\frac{\mu_\tau}{\sigma_k}\frac{\partial \overline{\rho} k}{\partial x_j}\right) \tag{16}$$

In figure 3, we compare the two models against the exact term. For M2, the models exhibit little differences, since flow property variations are relatively small. The discrepancies tend to increase at higher Mach numbers, with the uncorrected model underpredicting the peak in the buffer layer. Of note, the Catris-Aupoix and Otero models are essentially superposed for all cases. For the M12 case, all the models predict the position of the first peak in the buffer layer but underestimate its magnitude. The second peak position and magnitude are not predicted accurately by any of the models. Overall, based on a priori tests, the corrections do not seem to improve the agreement with the DNS significantly.

Next, we examine the k dissipation. When dealing with compressible flows, the dissipation ε can be expressed decomposed in two parts:

$$\overline{\rho}\varepsilon = \overline{\rho}\varepsilon_s + \overline{\rho}\varepsilon_d = \frac{\overline{\mu}}{\overline{\rho}}\overline{\rho\omega_i''\omega_i''} + \frac{4}{3}\frac{\overline{\mu}}{\overline{\rho}}\overline{\rho\vartheta''\vartheta''} \tag{17}$$

ω_i and ϑ being the vorticity components and the velocity divergence, respectively. The solenoidal dissipation ε_s coincides with the dissipation in the incompressible limit, whereas the dilatational dissipation ε_d appears only in compressible flows. For a two-equations model, the transport equations have to be adjusted to account for ε_d and this is done by considering a closure model for the term. A few models for ε_d have been proposed in the literature, mostly based on DNS databases for homogeneous isotropic turbulence or free-shear flows [17, 19, 14]. In both cases, the dilatation dissipation is assumed to take the general form [4]:

$$\varepsilon_d = \beta F(M_t)\varepsilon_s \tag{18}$$

with M_t the turbulent Mach number and β a modelling constant. Figure 4 reports profiles in semi-local scaling of the exact $\varepsilon_d/\varepsilon_s$ ratio from the DNS and its modelled counterpart according to the above-mentioned models. The analysis of such ratio from DNS allows to better quantify the magnitude of compressibility effects. ε_d assumes maximum values of the order of $\approx$ 4-5%ε_s at the wall, and becomes larger at the edge of the boundary layer where ε_s decays faster. Nevertheless, it is generally much smaller in the rest of the boundary layer; neglecting ε_d can therefore be considered a reasonable assumption. This does not seem to remain valid for M12, as the

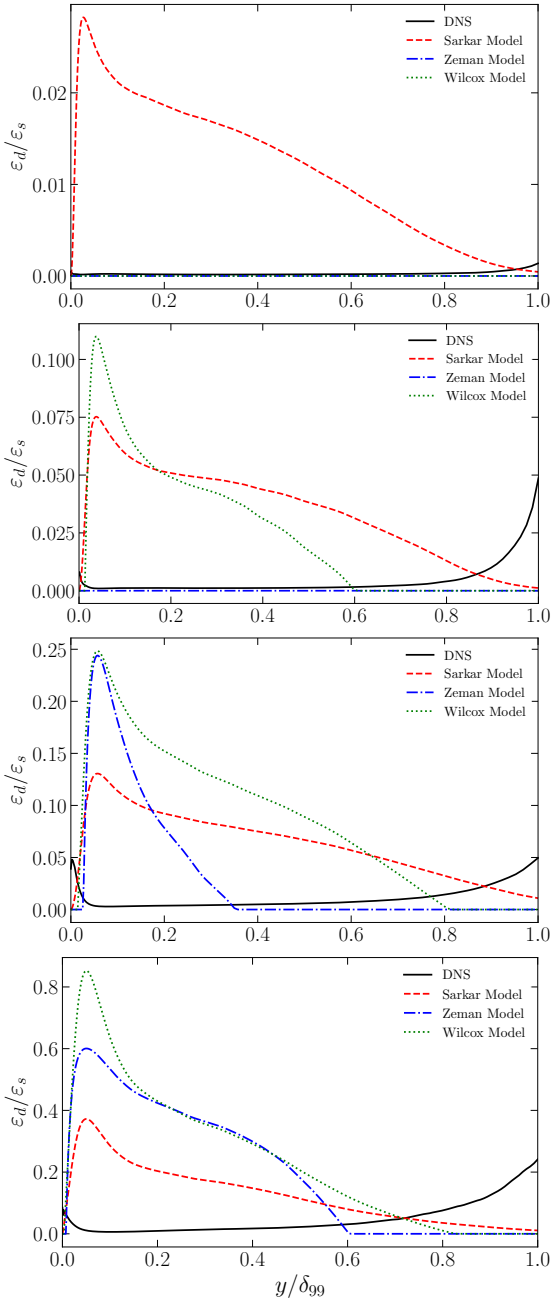

Figure 4: $\varepsilon_d/\varepsilon_s$ ratio of the exact term with the models. From top to bottom: M2, M6, M10C and M12.

wall cooling increases the significance of compressibility effects with $\varepsilon_d =\approx$ 7-8%ε_s. The results for the three models considered show their poor performance for all cases. This is a consequence of the simple functional relationship (18) assuming proportionality to ε_s through a function of M_t only, leading the models to peak where M_t peaks. Overall, the values tend to be largely overpredicted and the discrepancies increase with M_∞. As reported by [17], the role of models for ε_d mostly consists in increasing the overall dissipation of the RANS model, but all of them fail to describe correctly all its physical dependencies on flow parameters.

4.3 Turbulent heat flux

In this section we assess the behavior of constitutive relations for the turbulent heat flux term $q_j^t = \overline{\rho u_j'' h''}$ that appears in the averaged total energy equation. For the boundary layers at stake, we estimate an "exact" turbulent Prandtl number from the DNS data, as follows:

$$Pr_t \approx \frac{\overline{\rho u'' v''}}{\rho v'' T''} \frac{\partial \widetilde{T}}{\partial y} \left(\frac{\partial \widetilde{u}}{\partial y} \right)^{-1} \tag{19}$$

As mentioned, Pr_t is most often assumed to be constant and equal to 0.9 for TBL. More accurate results can be obtained by modelling Pr_t and letting it vary; one example is the empirical relation of Kays and Crawford [5]:

$$Pr_t = \left\{ \frac{1}{2Pr_{t\infty}} + \frac{CPe_t}{\sqrt{Pr_{t\infty}}} - (CPe_t)^2 \left[1 - \exp\left(-\frac{1}{CPe_t \sqrt{Pr_{t\infty}}} \right) \right] \right\}^{-1} \tag{20}$$

where $C = 0.3$, $Pr_{t\infty} = 0.9$ for air and $Pe_t = Pr\frac{\mu_t}{\mu}$ is a turbulent Peclet number. Another example is the model presented by Cebeci [3]

$$Pr_t = \frac{\kappa}{\kappa_\theta} \frac{1 - \exp(-y^+/A)}{1 - \exp(-y^+/B)} \tag{21}$$
$$\text{with} \quad B = \frac{1}{Pr^{1/2}} \sum_{i=1}^{5} C_i (\log_{10} Pr)^{i-1}$$

with $\kappa = 0.41$, $\kappa_\theta = 0.46$, $A = 26$, $C_1 = 34.96$, $C_2 = 28.79$, $C_3 = 33.95$, $C_4 = 6.3$, and $C_5 = -1.186$. In Figure 5 the comparison between the exact Pr_t, the models and $Pr_t = 0.9$ is shown. It appears that both the models and the constant assumption fail to accurately reproduce the trend of Pr_t for all the cases considered. The Kay-Crawford model provides a better representation of the near wall behavior, but neither model captures the "bump" located at $y/\delta_{99} < 0.2$, which is particularly accentuated for the M12 case. In the outer region, the exact values are below 0.9.

4.4 Mass transport and turbulence-chemistry interaction

In this section we assess models of unclosed terms in the species transport equations. We first focus on the turbulent mass transport term $\overline{\rho u_j'' Y_n''}$ (n being the number of species) for a turbulent boundary layer, and we plot the "exact" Schmidt numbers, computed from DNS data as:

$$Sc_{t,n} = \frac{\overline{\rho u'' v''} \partial \widetilde{Y}_n / \partial y}{\overline{\rho v'' Y_n''} \partial \widetilde{u} / \partial y} \tag{22}$$

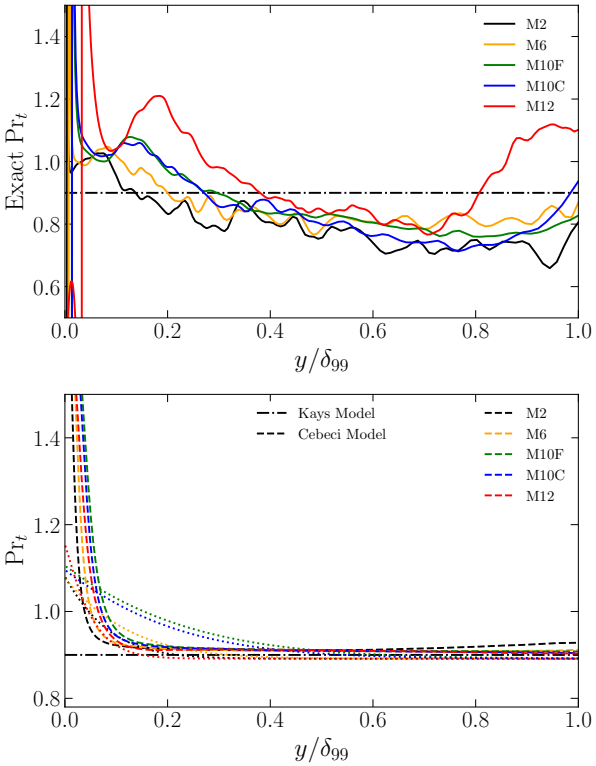

Figure 5: Exact Pr_t from DNS (top) and models from Kays and Cebeci (bottom).

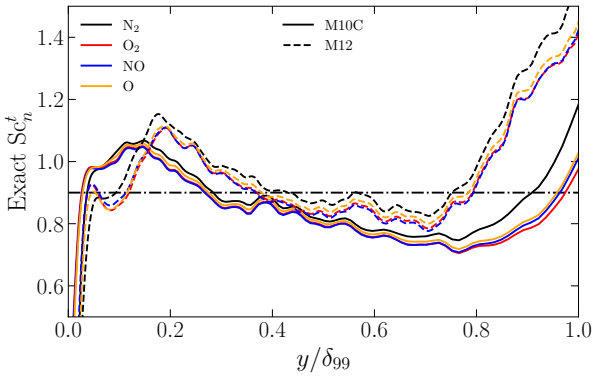

Figure 6: Exact Sc_t from DNS.

The results are reported in figure 6 for the species considered in the M10C and M12 cases. Similarly to Pr_t, $Sc_{t,n}$ exhibit a bump in the logarithmic region, more pronounced for M12, and are below the standard value in the outer region, the 0.9 value can be considered as an average across the boundary layer. The profiles do not differ much but the values are clearly affected by M_∞.

The influence of species mass fraction and temperature fluctuations on the species production rates, i.e. the intensity of turbulence-chemistry interactions (TCI), is quan-

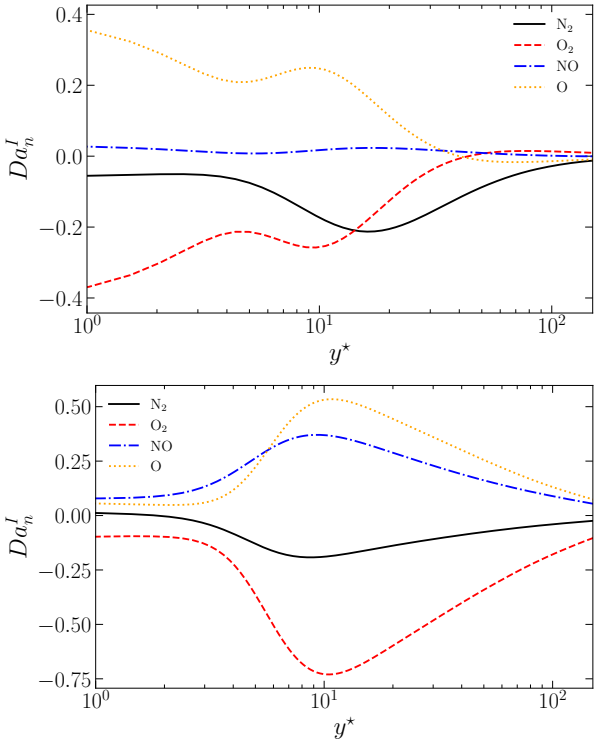

Figure 7: Species interaction Dahmköler number profile for the M10C and M12 simulations.

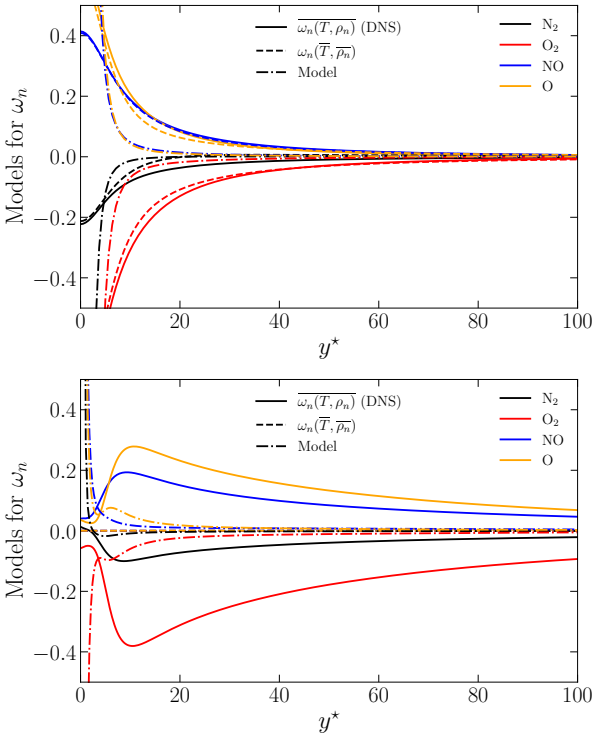

Figure 8: Species interaction Dahmköler number profile for the M10C and M12 simulations.

tified through the species interaction Dahmköler number:

$$Da_n^I = \frac{\overline{\omega_n\left(T,\rho_n\right)} - \omega_n\left(\overline{T},\overline{\rho_n}\right)}{\overline{\omega_n\left(T,\rho_n\right)}_w}, \qquad (23)$$

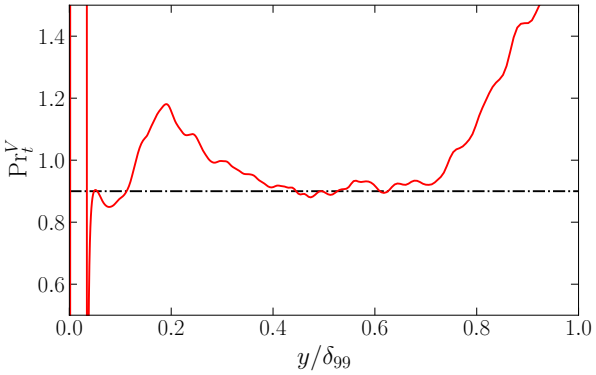

Figure 9: Exact Pr_t^{V} from DNS.

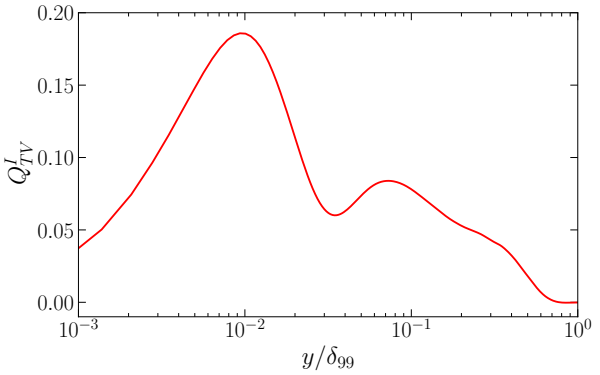

Figure 10: Translational-Vibrational source term interaction indicator for the M12 simulation.

where $\overline{\omega_n(T,\rho_n)}$ is a source term which represents the production or depletion of the n-th species in the mixture due to chemical reactions. This parameter represents the chemical production due to turbulent fluctuations caused by the non zero difference between $\overline{\omega_n(T,\rho_n)}$ and $\omega_n(\overline{T},\overline{\rho_n})$, since the expression for ω_n is nonlinear. A simplification often adopted in the RANS framework is to consider $\overline{\omega_n(T,\rho_n)} \approx \omega_n(\overline{T},\overline{\rho_n})$, which is an acceptable approximation only if the turbulence-chemistry interactions are limited. Due to the lack of models for the source terms in hypersonic TBL, an approach used for combustion applications is tested. We consider the model of [18], based on the Eddy Dissipation Concept (EDC); the chemical source term is then expressed as:

$$\overline{\omega_n} \approx \gamma^* \omega_n(\overline{T},\overline{\rho_n}). \tag{24}$$

Here, $\gamma^* \approx 9.7(\frac{\nu\varepsilon}{k^2})^{\frac{3}{4}}$ represents the fine-scale structure volume fraction, i.e. the fraction of the volume in which chemical reactions take place which is assumed to be in the region where turbulent kinetic energy is quasi-steady. Figure 7 shows the profile of Da_n^I for the different species of the mixture; N is not shown being present in negligible amounts. The indicator is overall small but assumes large values close to the wall for the adiabatic case M10C, and in the buffer region for the wall-cooled case M12, where turbulent fluctuations are significant. To gain a better overview of TCI, the profiles of $\overline{\omega_n(T,\rho_n)}$, $\omega_n(\overline{T},\overline{\rho_n})$ and the models are shown in figure 8. It can be observed that the assumption $\overline{\omega_n(T,\rho_n)} \approx \omega_n(\overline{T},\overline{\rho_n})$, is reasonably accurate while the EDC does not prove to be satisfactory.

4.5 Vibrational Turbulent Heat Flux and Turbulence-Vibrational Relaxation Interaction

We complete the analysis by investigating the behavior of unclosed terms in the averaged vibrational energy equation. As the heat flux was found to have an important part in the vibrational energy budget, modeling this term appears critical in a RANS approach. In [11], a gradient transport model is proposed, based on a vibrational turbulent Prandtl number Pr_t^{V} defined in [1]. Its "exact" value is extracted from DNS as:

$$Pr_t^{\mathrm{V}} = \frac{\overline{\rho u'' v''}\,\partial\widetilde{T}_{\mathrm{V}}/\partial y}{\overline{\rho v'' T_{\mathrm{V}}''}\,\partial\widetilde{u}/\partial y}, \tag{25}$$

such that the model reads:

$$\overline{\rho u_j'' e_V''} = \frac{\mu_t}{Pr_t^{\mathrm{V}}}\frac{\partial\widetilde{e}_V}{\partial x_j}. \tag{26}$$

The plot of figure 9 shows a behavior similar to Pr_t with a bump in the logarithmic region. In this case, the value 0.9 is reasonably well recovered in the outer region. Finally we assess the intensity of the interaction between turbulence and thermal relaxation, through the indicator introduced in [11]:

$$Q_{\mathrm{TV}}^I = \frac{\overline{Q_{\mathrm{TV}}(T,T_{\mathrm{V}},\rho,p,Y_n)} - Q_{\mathrm{TV}}\left(\widetilde{T},\widetilde{T_{\mathrm{V}}},\overline{\rho},\overline{p},\widetilde{Y_n}\right)}{\overline{Q_{\mathrm{TV}}^{\max}}}, \tag{27}$$

where $\overline{Q_{\mathrm{TV}}}$ is a source term accounting for vibrational energy production/depletion due to translational-vibrational energy transfers and $\overline{Q_{\mathrm{TV}}^{\max}}$ is the maximum wall-normal value of at the selected station. Figure 10 shows differences up to $\approx 15\%$ in the inner layer, indicating a strong interaction between turbulence and thermal non-equilibrium. While for $\dot{\omega}$ a few models do exist, allowing to quantify the intensity of TCI, no models for $\overline{Q_{\mathrm{TV}}}$ are available, which is potentially critical for RANS modeling of hypersonic flows out of thermal equilibrium.

5. CONCLUSIONS

We reported a priori tests of RANS closures and compressibility corrections available in literature for various TBL configurations. Reference data were extracted from DNS databases ranging from the supersonic to the hypersonic regime, including conditions of thermochemical non equilibrium. Direct extensions of incompressible

closures for unclosed terms in the turbulent kinetic energy equation are show to be inadequate. Unfortunately, the few compressibility correction available in the literature are not found to capture DNS data much better, especially at high Mach numbers and in presence of wall cooling. The gradient approximation, commonly used to model turbulent heat fluxes, was found unable to predict the stream-wise component of various terms, pointing out limitations in the Reynolds analogy, on which the model is based. Similar results were found for the vibrational turbulent heat flux, while models adapted from the ones for turbulent heat fluxes were shown to provide acceptable results. Other closure approaches specific to this term may be developed. High-temperature effects were found not to alter the validity of classical closure models. Nevertheless, the new unclosed terms in the species and vibrational energy equations need to be modeled accordingly. Further work on many aspects of compressible turbulence modelling is required, in particular in the development of closures that properly account for compressibility, for instance by means of machine learning techniques.

REFERENCES

[1] A. Baranwal, D. A. Donzis, and R. D. Bowersox. Vibrational turbulent prandtl number in flows with thermal non-equilibrium. In *AIAA Scitech 2020 Forum*, page 2052, 2020.

[2] S. Catris and B. Aupoix. Density corrections for turbulence models. *Aerospace Science and Technology*, 4(1):1–11, 2000.

[3] T. Cebeci. A model for eddy conductivity and turbulent Prandtl number. *Journal of Heat Transfer*, 95:227–234, 1973.

[4] T. B. Gatski. Modeling compressibility effects on turbulence. In *New Tools in Turbulence Modelling: Les Houches School, May 21–31, 1996*, pages 73–104. Springer, 1997.

[5] W.M. Kays, M.E. Crawford, and B. Weigand. *Convective heat and mass transfer*. McGraw–Hill, 1980.

[6] F. R. Menter. Improved two-equation k-omega turbulence models for aerodynamic flows. Technical report, 1992.

[7] G. Otero, A. Patel, R. Diez, and R. Pecnick. Turbulence modelling for flows with strong variations in thermo-physical properties. *Journal of Heat and Fluid Flow*, 823:R1, 2018.

[8] G. J. Otero Rodriguez. *Computational fluid dynamics for non-conventional power cycles: Turbulence modelling of supercritical fluids and simulations of high-expansion turbines*. PhD thesis, TU Delft, 2021.

[9] C. Park. Two-temperature interpretation of dissociation rate data for N2 and O2. In *26th Aerspace Sciences Meeting*, page 458, 1988.

[10] D. Passiatore, L. Sciacovelli, P. Cinnella, and G. Pascazio. Finite-rate chemistry effects in turbulent hypersonic boundary layers: A direct numerical simulation study. *Physical Review Fluids*, 6(5):054604, 2021.

[11] D. Passiatore, L. Sciacovelli, P. Cinnella, and G. Pascazio. Thermochemical non-equilibrium effects in turbulent hypersonic boundary layers. *Journal of Fluid Mechanics*, 941:A21, 2022.

[12] R. Pecnick and A. Patel. Scaling and modelling of turbulence in variable property channel flows. *Journal of Fluid Mechanics*, 95:227–234, 2017.

[13] C. Roy and F. Blottner. Review and assessment of turbulence models for hypersonic. *Progress in Aerospace Sciences*, 42:469–530, 2006.

[14] S. Sarkar, G. Erlebacher, M. Y. Hussaini, and H. O. Kreiss. The analysis and modelling of dilatational terms in compressible turbulence. *Journal of Fluid Mechanics*, 227:473–493, 1991.

[15] L. Sciacovelli, X. Gloerfelt, D. Passiatore, P. Cinnella, and F. Grasso. Numerical investigation of high-speed turbulent boundary layers of dense gases. *Flow, Turbulence and Combustion*, 105:555–579, 2020.

[16] L. Sciacovelli, D. Passiatore, P. Cinnella, and G. Pascazio. Assessment of a high-order shock-capturing central-difference scheme for hypersonic turbulent flow simulations. *Computers & Fluids*, 230:105134, 2021.

[17] D. C. Wilcox. Dilatation-dissipation corrections for advanced turbulence models. *AIAA journal*, 30(11):2639–2646, 1992.

[18] Z. Xiang, S. Yang, S. Xie, J. Li, and H. Ren. Turbulence–chemistry interaction models with finite-rate chemistry and compressibility correction for simulation of supersonic turbulent combustion. *Engineering Applications of Computational Fluid Mechanics*, 14(1):1546–1561, 2020.

[19] O. Zeman. Dilatation dissipation: the concept and application in modeling compressible mixing layers. *Physics of Fluids A: Fluid Dynamics*, 2(2):178–188, 1990.